https://doi.org/10.1016/j.jpowsour.2020.228916

Critical roles of microstructure and interphase on the stability of microsized germanium anode

Jian-Qiu Huang[a, #], Xuyun Guo[a, #], Jiaqiang Huang[a], Hong Tan[a, b], Xiaoqiong Du[a, b], Ye Zhu[a,*], and Biao Zhang[a,b,*]

[a]*Department of Applied Physics, the Hong Kong Polytechnic University, Hung Hom, Hong Kong, China.*

[b]*The Hong Kong Polytechnic University Shenzhen Research Institute, Shenzhen, China*

[#]*These authors contribute equally to this work.*

**Corresponding authors: Biao Zhang. Email: biao.ap.zhang@polyu.edu.hk; Ye Zhu. Email: ye.ap.zhu@polyu.edu.hk.*

Abstract

Creating a certain degree of porosity is a widely adopted strategy in maintaining the cyclic stability of alloy anodes in Li-ion batteries (LIBs). The free space provided by the nanopores enables to partly alleviate the large strains during lithiation for increasing structural integrity. Instead of fabricating a nanostructured electrode with pre-designed pores, nanopores are *in-situ* created during lithiation/de-lithiation of Ge electrodes, enabling the direct utilization of microsized Ge particles. Assisting by scanning transmission electron microscopy (STEM), we systematically explore the microstructure evolution of Ge particles during cycling. It reveals the vital role of pore development, which is closely related to the solid electrolyte interphase (SEI), in maintaining the stable cyclic performance. The nanostructure of SEI is further resolved by cryo-transmission electron microscopy (cryo-TEM), which suggests that the amorphous inorganic component is essential to the fast kinetics for inducing sufficient porosity. Compared to the classic lithium hexafluorophosphate ($LiPF_6$) salt in the electrolyte, the lithium difluoro(oxalato)borate (LiDFOB) shows great advantages in constructing a highly ionic

conductive SEI layer for facilitating the nanopore growth. This work demonstrates the critical roles of interphase and the resulted microstructure in stabilizing the alloy microparticles.

Keywords: microsized Ge anode; nanopores; electrode-electrolyte interphase; Cryo-TEM; Li-ion batteries

1. Introduction

The practical application of high-capacity alloy anodes would significantly increase the energy densities of current Li-ion batteries (LIBs). These anodes such as Si, Ge, and Sn possess several times higher theoretical capacities than graphite but suffer from severe capacity fading due to the volume expansion upon Li ion uptake [1]. Downsizing the particles into nanoscale is among the most effective strategies to improve cyclic stability [2, 3]. The nanostructured electrode usually has multi-scale pores, which provide free volume to sustain the swelling of the electrode. Hybridization with nanocarbon materials, an approach that has been widely adopted, could further increase the cyclic stability and rate capability [4-6]. Nevertheless, a large initial irreversible capacity is observed in these nanomaterials due to the copious formation of solid electrolyte interphases (SEIs) on the high-surface-area electrode [7, 8]. The tap density of the nanosized materials should also be improved to obtain a satisfactory volumetric energy density.

Microsized particles are desired because of their easy fabrication, high tap density, and low surface area. Despite these advantages, the large size aggravates the internal stress upon lithiation, resulting in the fracture and disconnection of particles and finally leading to severe capacity degradation. Up to now, several promising tactics have been proposed to circumvent the isolation of broken particles, including i) Be confined in the hollow carbon sphere. The carbon shell not only facilitates the charge transfer but also preserves the integrity of the electrode [9]. ii) Design a highly elastic binder. The mechanical strength of the binder is

enhanced through functionalization to sustain the volume change of particles, thus avoiding the pulverization of active materials [10]. iii) Construct robust electrode-electrolyte interphases [11, 12]. Several examples in Na-ion and K-ion batteries have been discovered. Microsized Sn [13] and Bi [14, 15] show extremely stable performance with the assistance of glyme-based electrolyte, which helps the formation of dense SEIs to constrain the cracked particles. The extension to LIBs has been partly limited by the low solubility of lithium salts in glyme solvent. Very recently, by utilizing cyclic ether solvent, Wang et al. stabilize the Si, Al, and Bi microsized anodes in LIBs through constructing LiF-rich SEI [16]. Nevertheless, the stability of ether at high voltages remains a great challenge for the practical application in full cells.

Ge anode receives less attention than other alloy anodes because of its relatively high cost. The downside is partly offset by the high capacity and fast Li ion diffusion coefficient, making it a promising candidate for high-energy and high-power batteries. Moreover, previous studies showed that nanopores tend to form in single Ge nanowire [17, 18], which is beneficial to alleviating internal stress. An intriguing question is whether sufficient pores could be developed in microsized particles, so as to assist the stabilization of the electrode if the particles do not collapse during pore propagation. In this study, Ge particles with an average size of 1.4 μm are investigated. The microstructural evolution during cycling is revealed by scanning transmission electron microscopy (STEM). To stabilize the cyclic performance of microsized particles, a vigorous SEI is built in the traditional carbonate electrolyte aided by the lithium difluoro(oxalato)borate (LiDFOB) salt. Cryo-transmission electron microscopy (cryo-TEM) and electron energy loss spectroscopy (EELS) are employed to disclose the detailed structure of SEI for gaining insights into its "structure-property" relationships.

2. Experimental Section

2.1. Preparation of Ge electrodes and $LiCoO_2$ electrodes

Ge (Macklin, ~200 μm, 99.999%) was mixed with carbon black, carbon fibers, and carboxymethylcellulose sodium (CMC) (Sigma-Aldrich, average Mw ~700,000) in a weight ratio of 7:1:1:1 by ball milling for 4 h in an argon atmosphere at a speed of 360 r min^{-1}. The as-prepared mixture was then added to deionized (DI) water and magnetically stirred. The obtained slurry was cast onto a copper foil and dried at 60 °C in an air-circulated oven. The $LiCoO_2$ electrodes were prepared by mixing commercial $LiCoO_2$ powders (Battflex Corporation, Wuhan), carbon black, and polyvinylidene difluoride (PVDF) with a weight ratio of 8:1:1 in N-methy1-2-pyrrolidone (NMP) with magnetically stirring. The slurry was then applied on an aluminum foil and dried in the oven. The electrodes were cut into discs with a diameter of 14 mm.

2.2. Characterization

All the cycled electrodes were washed using dimethyl carbonate (DMC) to remove the remaining salt residuals before characterization. The morphologies of electrodes were examined on scanning electron microscopes (SEM, JEOL JSM-6335F, and TESCAN VEGA3). The crystalline phases of the materials were detected on an X-ray diffraction (XRD) system (Rigaku SmartLab) with Cu Ka radiation source with a scan rate of 2° min^{-1}. In-situ XRD test was conducted using a Swagelok-type cell. The active materials were directly cast on a Beryllium window (supplied by Goodfellow, with an electrical conductivity of 303 S cm^{-1}), serving as both a transparent X-ray window and a current collector [19, 20]. For ex-situ XRD, the cycled cells were disassembled in the glove box. The cycled electrode was placed in the Swagelok-type cell with active materials facing the Beryllium window for measurement. X-ray photoelectron spectroscopy (XPS, PHI5600 by Physical Electronics, Inc.) was conducted using a monochromatic Al Ka X-ray at 14 kV. All transmission electron microscopy (TEM) and scanning TEM (STEM) were performed using JEOL JEM-2100F operated at 200 kV, equipped with a Gatan Enfina electron energy loss spectrometer (EELS). Spectrum imaging of

EELS was carried out under 200 kV accelerating voltage with a 13 mrad convergence angle for the optimal probe condition. Energy dispersion of 1.0 eV per channel and 21 mrad collection angle were set up for EELS. HAADF images were acquired with an 89 mrad inner angle simultaneously. The Ge, C, Li, O, F, B, and P intensity maps were extracted from the EELS spectrum image by integrating across the energy windows of 1217-1320 (Ge L2,3 edge), 284-302 (C K edge), 55-63 (Li K edge), 532-546 (O K edge), 685-710 (F K edge), 188-207 (B K edge), and 132-145 (P K edge) eV, respectively. To minimize the beam damage to the frail SEI, we utilize cryo-TEM and cryo-EELS to examine their pristine morphology, lattice image, and chemical composition. Prior to observation, the sample was transferred to a double tilt nitrogen cooling holder (Gatan, model 636) for cryo-EM study, operated under ~-175 ^{o}C. The system was stabilized for at least 40 min after adding the liquid nitrogen to minimize the vibration.

2.3. Electrochemical tests

For half cells, CR2032 coin cells were assembled using the Li foil as the anode, the glass fiber (Whatman, GF/D) as the separator, and the Ge electrode as the cathode. The mass of the active materials on individual electrodes was about 0.8-1.0 mg cm^{-2}. To investigate the electrolyte effect, 1 M Lithium hexafluorophosphate ($LiPF_6$) or 1 M Lithium difluoro(oxalato)borate (LiDFOB) in ethylene carbonate (EC) and dimethyl carbonate (DMC) at a volume ratio of 1:1 was used as the electrolyte. The half cells with the two electrolytes were discharge/charge cycled between 0.01 and 1.5 V on a LAND 2001 CT battery tester at room temperature. To replace the corroded Li anode, the cell with LiDFOB at charged state was disassembled in the glove box and re-assembled using a fresh Li foil. A voltage cuttoff of 2.0-4.25 V was applied on the full Ge-$LiCoO_2$ batteries with the two electrolytes. The weight ratio of Ge and $LiCoO_2$ in full cells is around 1:10 to ensure a 5% excess of anode capacity for avoiding Li plating. The cell capacity of the full cell was calculated based on the weight of the cathode material in this

work. To avoid the interference of side reactions from the counter electrode side, three-electrode Swagelok cells were fabricated for electrochemical impedance spectra (EIS) measurements. The EIS results were obtained at a constant perturbation amplitude of 5 mV in the frequency range between 0.01 Hz and 100k Hz.

3. Results and discussion

3.1. Electrochemical performance

Commercial Ge microparticles were directly used as active materials. Carbon black and carbon fibers with equal amounts were incorporated as conductive additives, which proves effective in establishing three-dimensional conductive networks [20-22]. The Ge particles, carbon additives, and carboxymethylcellulose sodium (CMC) binder were mixed by ball milling. After one-hour mixing, uniform dispersion of carbon additives is achieved. However, the enlarged scan electron microscopy (SEM) image shows the presence of bare surfaces on Ge particles (**Fig. S1**), necessitating longer mixing time. A four-hour ball milling is conducted to ensure close contact between the Ge particles and carbon additives. **Fig. 1a** and **1b** manifest that the surface of Ge particles is covered by carbon black while carbon fibers bridge the particles to ensure a fast electron transfer path. The microsized nature of the particles is remained due to the low energy of planetary ball milling. An average size of 1.4 μm is obtained with a deviation of 0.5 μm (inset of **Fig. 1a**). The crystallinity of Ge is also maintained, as shown in the XRD spectra of **Fig. S2**. The crystal structure of Ge (inset of **Fig. S2**) is similar to diamond and Si that belongs to a face-centered cubic system. A tiny amount of GeO_2 is observed in both pristine and ball-milled samples, due possibly to the oxidation of Ge particles during the manufacture.

The electrochemical performance was evaluated by coin cells in two electrolyte systems. In both electrolytes, representative carbonate solvents, i.e., a mixture of ethylene carbonate/dimethyl carbonate (EC/DMC) (1:1 in volume), are adopted to be compatible with

practical applications. In addition to classic lithium hexafluorophosphate ($LiPF_6$) salt, LiDFOB salt is also employed to help build robust electrode/electrolyte interphases. An electrolyte additive, LiDFOB salt has been demonstrated beneficial to the formation of electrochemical stable cathodic electrolyte interphase (CEI) for working at a high voltage [23, 24], to the construction of uniform SEI for smooth Li plating [25] and the stabilization of several promising anodes [26-28]. Its effect in stabilizing alloy anodes accompanying high volume expansion has yet to be explored. The voltage profiles of Ge anodes in LiDFOB electrolyte (1 M LiDFOB in EC/DMC) is shown in **Fig. 1c**. Two plateaus located at around 0.30 V and 0.16 V appear in the dQ/dV plot (inset of **Fig. 1c**) of the 1st discharge curve, giving rise to an accumulative capacity of 1665 mAh g^{-1}. Accordingly, the 1st charge profile presents two oxidation plateaus at 0.47 and 0.63 V, resulting in a charge capacity of 1299 mAh g^{-1}. It gives an initial Coulombic efficiency of 78%. The plateaus become less visible in the 2nd cycle. A sloping feature is observed in the discharge, while the two plateaus merge into one upon charge. The voltage profiles of the following cycles resemble those in the 2nd cycle. It suggests two distinct reaction paths in the initial cycle and the rest, which will be discussed later. The voltage profiles in $LiPF_6$ electrolyte (1 M $LiPF_6$ in EC/DMC), as shown in **Fig. 1d**, are identical to those in LiDFOB one, indicating the change of salt has a negligible effect on the phase transition process. The initial Coulombic efficiency in $LiPF_6$ electrolyte has a slightly higher value of 83%, as a reflection of the difference in the SEI formation with the two salts.

Both the structure of electrodes and the electrolyte significantly affect the cyclic performance of microsized Ge anodes. In **Fig. S3**, the electrode made from a one-hour ball milled sample undergoes a fast capacity fading. The capacity quickly decreases to 646 mAh g^{-1} in 50 cycles at a current density of 0.1 C. The stability is greatly improved for four-hour-milled sample in LiDFOB electrolyte with slightly reduced particle size. A capacity of 1211 mAh g^{-1} is attained after 200 cycles, accounting for 88% of its capacity in the 2nd cycle. It

signifies the importance of attaching the carbon additives to the surface of microsized particles, which enhances the charge transfer and improves the cyclic stability. Surprisingly, the stability in the traditional $LiPF_6$ electrolyte is much worse as shown in **Fig. 1e**. It has a similar capacity of 1296 mAh g^{-1} in the 2nd cycle but only sustains for 70 cycles, after which a fast capacity degradation occurs. The above observation is further confirmed in the long-cyclic tests at a high current density of 1 C as shown in **Fig. 1f**. The cyclic stability is greatly improved with the shift of electrolyte salt from $LiPF_6$ to LiDFOB. A capacity retention of 69% is obtained after 300 cycles for the four-hour milled electrode. A fluctuation of Coulombic efficiency occurs in around 50 cycles, which is ascribed to the corrosion of Li metal counter electrode as proved by the optical image of the cycled Li electrode (**Fig. S4**). The Li corroded anode was replaced by a fresh one for the cell with LiDFOB electrolyte at 70th and 200th cycle, as shown in **Fig. 1f**. The efficiency recovers to over 99% with the replenished Li foil. Noteworthy that it is not an obstacle in practical cells since metallic Li should be avoided in Li-ion full battery. In comparison, the cell in $LiPF_6$ electrolyte has similar behaviors as that cycled at 0.1 C, which exhibits a fast capacity fading after 30 cycles.

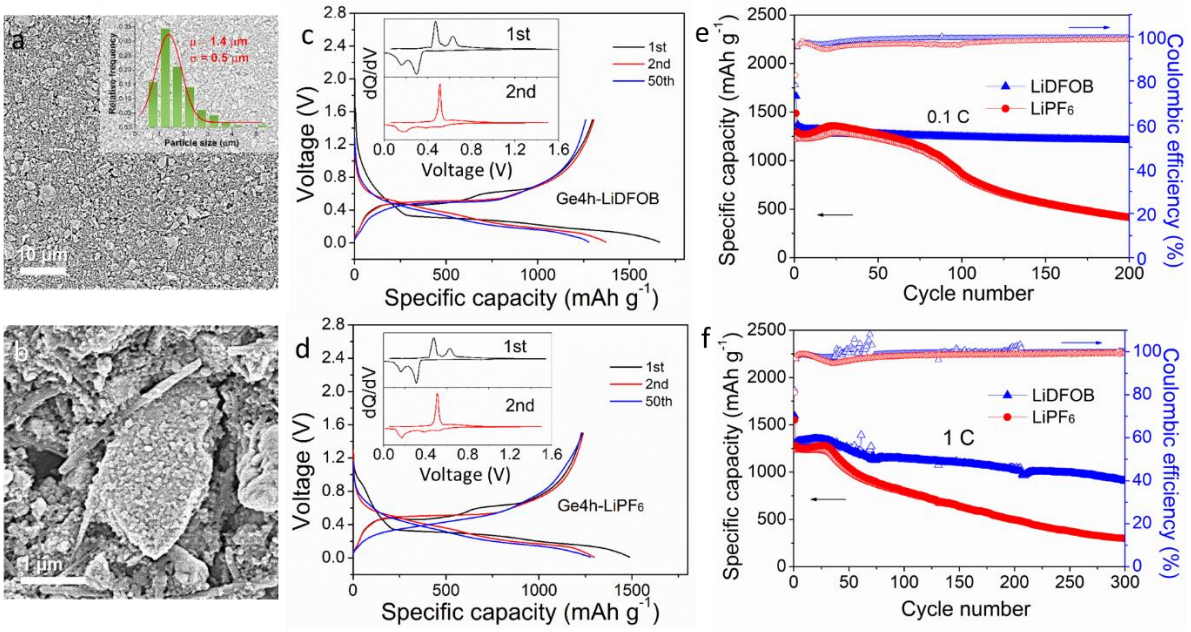

Fig. 1. Morphology and electrochemical performance. (a), (b) SEM images of four-hour milled

electrodes with a histogram showing the distribution of Ge particle size in the inset of (a); charge and discharge curves of four-hour milled electrodes in (c) LiDFOB and (d) $LiPF_6$ electrolytes with dQ/dV plots in the inset; cyclic performance of four-hour milled electrodes at (e) 0.1 C and (f) 1 C in LiDFOB and $LiPF_6$ electrolytes.

3.2. Structural and morphological evolution

To explore the reasons behind the variation of voltage profiles in the first two cycles, the phase transformation of Ge was investigated by *in-situ* X-ray diffraction (XRD) measurement using a Swagelok-type cell equipped with a Beryllium window as both a transparent X-ray window and a current collector. The lithiation and de-lithiation process was conducted at a current density of 0.1 C (corresponding to 160 mAh g^{-1}). The voltage profiles and the representative XRD patterns at different charge/discharge states were plotted in **Fig. 2**. Four reflexes at 27.3°, 45.3°, 53.8° and 66.1° presented in the fresh electrode are indexed to the (111), (220), (311) and (400) planes of pristine Ge, respectively. There are not any clear changes until discharged to 0.4 V, suggesting that the SEI formation is the major activity at the initial stage. The LiDFOB salt decomposes at around 1.2 V, while the EC/DMC solvents degrade at around 0.8 V [28, 29]. Afterward, the intensities of Ge diffraction reflexes gradually weaken without the appearance of new reflexes. It indicates the formation of amorphous Li_xGe in the second stage of first discharge, in agreement with the previous study [30]. Once the voltage arrives at 0.1 V, tiny reflexes at 20.2°, 23.4°, and 26.1° originating from $Li_{15}Ge_4$ are observed. Their intensities are significantly enhanced with continuous lithiation to 0.01 V, reflecting that the crystallization of $Li_{15}Ge_4$ from amorphous Li_xGe is the last step in the initial reduction. Upon charging, the $Li_{15}Ge_4$ phase rapidly disappears. Only a small reflex is left at 0.6 V, and no crystalline phase presents when charged to 1.0 V. Out of our expectation, the reflexes of Ge are not recovered even after full extraction of Li ions at 1.5 V. Therefore, the 2nd discharge

starts with amorphous instead of crystalline Ge, leading to distinct voltage profiles with 1st cycle (**Fig.1c** and **1d**). The amorphous state is almost maintained throughout the whole discharge. Only one small reflex of $Li_{15}Ge_4$ at 23.4° appears at the end of discharge, which vanishes in the charging process and recovers to a disordered structure at 1.5 V. The gradual amorphization of Ge during cycling is also confirmed by *ex-situ* XRD. The patterns after three and fifty cycles in **Fig. S5** indicate the absence of any crystallized phases.

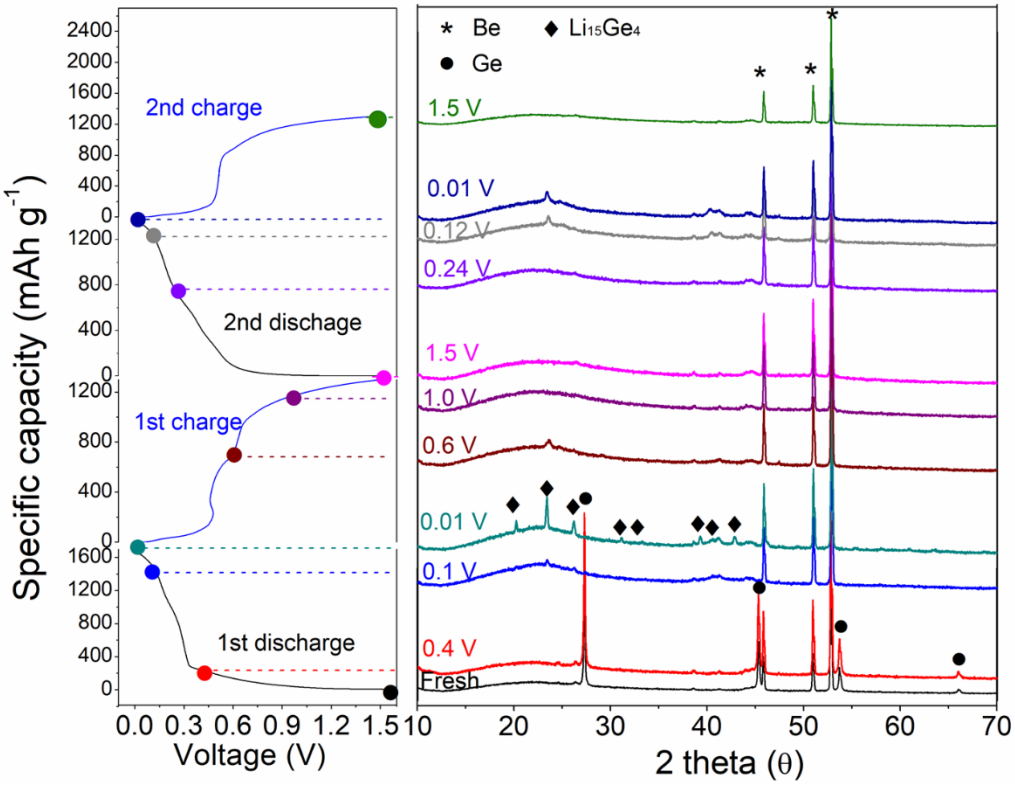

Fig. 2. Phase transition process. *In-situ* XRD patterns of the Ge electrode in LiDFOB electrolyte in the first two cycles.

The above amorphization process would significantly affect the morphology of Ge particles. The pulverization of particles is one of the primary reasons for the capacity fading of alloy anodes. The morphology evolution of Ge is monitored by STEM to detect the internal structure of particles. The pristine Ge has an intact form without any trace of cracks, indicating the ball milling does not bring damage to the particles (**Fig. 3a**). The well-defined crystal

lattices in high-resolution TEM (HRTEM) and sharp diffraction spots in selected area electron diffraction (SAED) pattern in **Fig. 3b** reaffirm the high crystallinity of Ge particles before cycling. After three cycles in both electrolytes, a great number of pores are produced inside the particles (**Fig. 3c** and **3d**). The porosity in the electrodes after 50 cycles is significantly increased, and a flower-like morphology is captured after 300 cycles (**Fig. 3e** and **3g**). Compared to the electrodes cycled in $LiPF_6$ electrolyte (**Fig. 3f** and **3h**), the development of nanopores in LiDFOB one appears to be more prominent. Sufficient porosity plays a key role in maintaining structural stability. With a quick pore growth, a porous Ge network is built in LiDFOB electrolyte, providing free space for the volume swelling. In contrast, fracture of particles occurs before adequate pores are generated when cycling in $LiPF_6$ electrolyte (**Fig. 3f** and **S6**, label by yellow dashed curve). After 300 cycles, a considerable number of fragments are observed, explaining the fast capacity degradation (**Fig. 3h** and inset, highlight in yellow dashed circle).

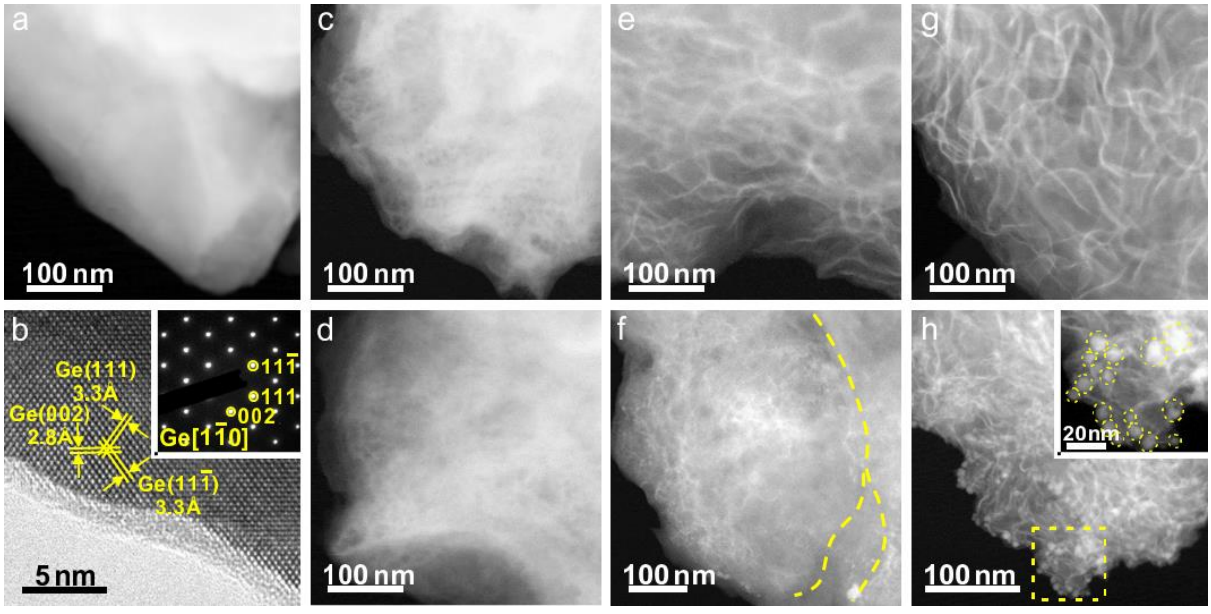

Fig. 3. Microstructure evolution. (a) STEM and (b) HRTEM with SAED as inset images of the pristine Ge; STEM images of Ge in LiDFOB electrolyte after (c) 3, (e) 50 and (g) 300 cycles; STEM images of Ge in $LiPF_6$ electrolyte after (d) 3, (f) 50 and (h) 300 cycles.

The formation of nanopores has been well observed in Ge nanowires, which includes the emerging of vacancies during de-lithiation and their agglomeration into tiny voids. [17] Therefore, pore development would largely rely on Li ion diffusivity. Electrochemical impedance spectroscopy (EIS) is adopted to compare the Li ion diffusion coefficient in the two electrolyte systems. Since the corrosion of Li metal occurs in the coin cell (**Fig. S4**), a three-electrode system, as schematically shown in the inset of **Fig. 4**, is built up to avoid the interference of the counter electrode. The EIS of the electrodes at different states, i.e., pre- and post- cycles, are collected and shown in **Fig. S7**. The data are fitted using equivalent circuit showing in the inset, where the response at high frequencies is generally ascribed to the fast processes occurring at thin SEI layer, the reaction at medium frequencies is related to the charge transfer at electrode/electrolyte interphase, and the points at low frequencies are associated with the Warburg impedance [31, 32]. The values are summarized in **Table S1** and **S2** and presented in **Fig. 4** and **S8**. It shows that the Li diffusivity in the bulk region, according to Warburg impedance, is quite close in the two electrolyte systems. It does not come as a surprise, as the changing of salt in the electrolyte barely affects the phase transformation process. Instead, it affects mostly on the SEI layer, and charge transfer through the interphase. Both the R_{sei} and R_{ct} are much reduced when shifting from $LiPF_6$ to LiDFOB electrolyte. Moreover, the two values keep almost constant along with cycles in the LiDFOB system, while the ones in $LiPF_6$ counterpart significantly increase after 30 cycles. Therefore, the sluggish process at the interphases of $LiPF_6$ electrolyte restricts the rapid extraction of Li ions from creating sufficient voids for fast pore development.

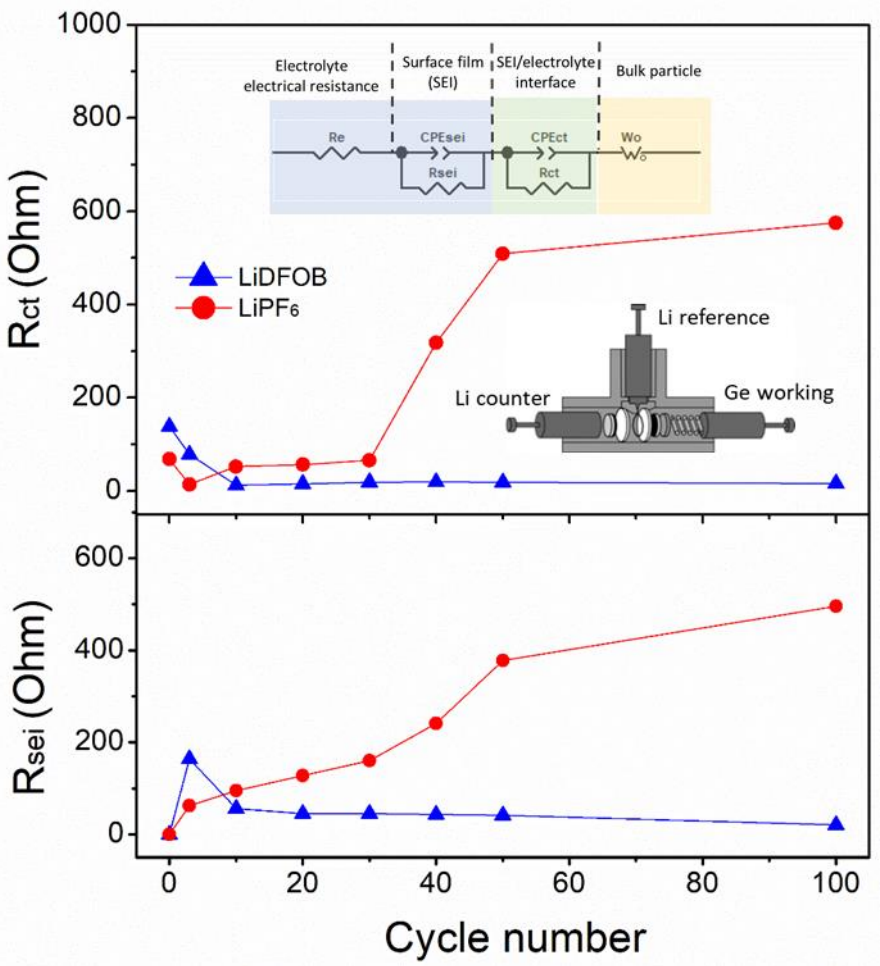

Fig. 4. The resistance of the electrodes. R_{sei} and R_{ct} values of Ge electrodes after different cycles in LiDFOB and $LiPF_6$ electrolytes. Schematic of the three-electrode system and the equivalent circuit for the EIS fitting are given in the insets.

3.3. Resolving the structure of SEI

To gain insights into how the salt of electrolyte modifies the interphase, X-ray photoelectron spectroscopy (XPS) was applied on the Ge electrodes after three cycles to investigate the chemical species in SEIs. Binding energies were calibrated using the C 1s at 284.8 eV, representing C=C bonds. The results indicate the SEI consists of organic alkyl carbonates and inorganic constituents. Deconvoluted XPS spectra of C 1s and O 1s in **Fig. S9a** and **S9b** suggest the organic species for the SEIs formed in both electrolytes are akin, which consists of mainly lithium alkyl carbonates $ROCO_2Li$ [33], but different inorganic components are observed in F

1s spectra (**Fig. S9c**). While Li_2CO_3-like particles are found in both the cases, rich LiF species are presented in the one cycled in LiDFOB electrolyte, which is thought to be beneficial to improving the ionic conductivity [25].

Apart from the compositions, the distribution and morphology of the components would also affect the ionic conductivity of SEI. The beam-sensitive nature of SEIs makes it challenging to give a close examination, a recently developed cryo-TEM is adopted to resolve the nanostructures [34]. After three cycles in both electrolytes, the particles are encapsulated in a thick SEI layer of tens of nanometers (**Fig. S10** and **S11**). The SEI in LiDFOB electrolyte is amorphous without any trace of crystalline structures being observed under HRTEM and SAED (**Fig. S10b** and **S10c**). For the case in $LiPF_6$ electrolyte, the HRTEM image in **Fig. S11c** shows that the SEI has an amorphous matrix comprised of organic carbonates. Both HRTEM and SAED (**Fig. S11b** inset) suggest the presence of polycrystalline particles in the SEI. According to the characteristic d-spacings, the crystals could be assigned to Li_2CO_3, which is consistent with XPS results. The contrast becomes more apparent in the samples after 50 cycles (**Fig. 5a-5f**). The one in LiDFOB electrolyte shows a decrease in the crystallinity. A full amorphous structure is captured in SAED (**Fig. 5b** and **5c**). The restriction of the crystallization and growth of inorganic particles resides in the capping effect of LiDFOB, due to the presence of oxalate groups [25]. In contrast to it, the crystallinity of inorganic particles is well preserved, but the size of Li_2CO_3 (circled in **Fig. 5f**) grows slightly larger in the SEI of the electrode cycled in $LiPF_6$ electrolyte, as compared to the samples after 3 cycles (**Fig. S11c**). The poor crystallinity of inorganic components in the SEI under LiDFOB electrolyte is partly responsible for the enhanced ionic conductivity. A similar phenomenon is observed in the SEI formed in Na-ion batteries [13] and also reported on Li_2O_2 case [35], whose ionic conductivity could be improved by twelve orders of magnitude through amorphization. Another factor, which may affect the Li ion conductivity of the SEI, is the homogeneity. The elemental distribution is

mapped by cryo-EELS. It shows a homogeneous composition in both electrolytes (**Fig. 5g** and **S12**). Therefore, the nature of the inorganic components and their crystallinity play vital roles in the ionic conductivity at the interphase, which controls the development of the pores during cycling.

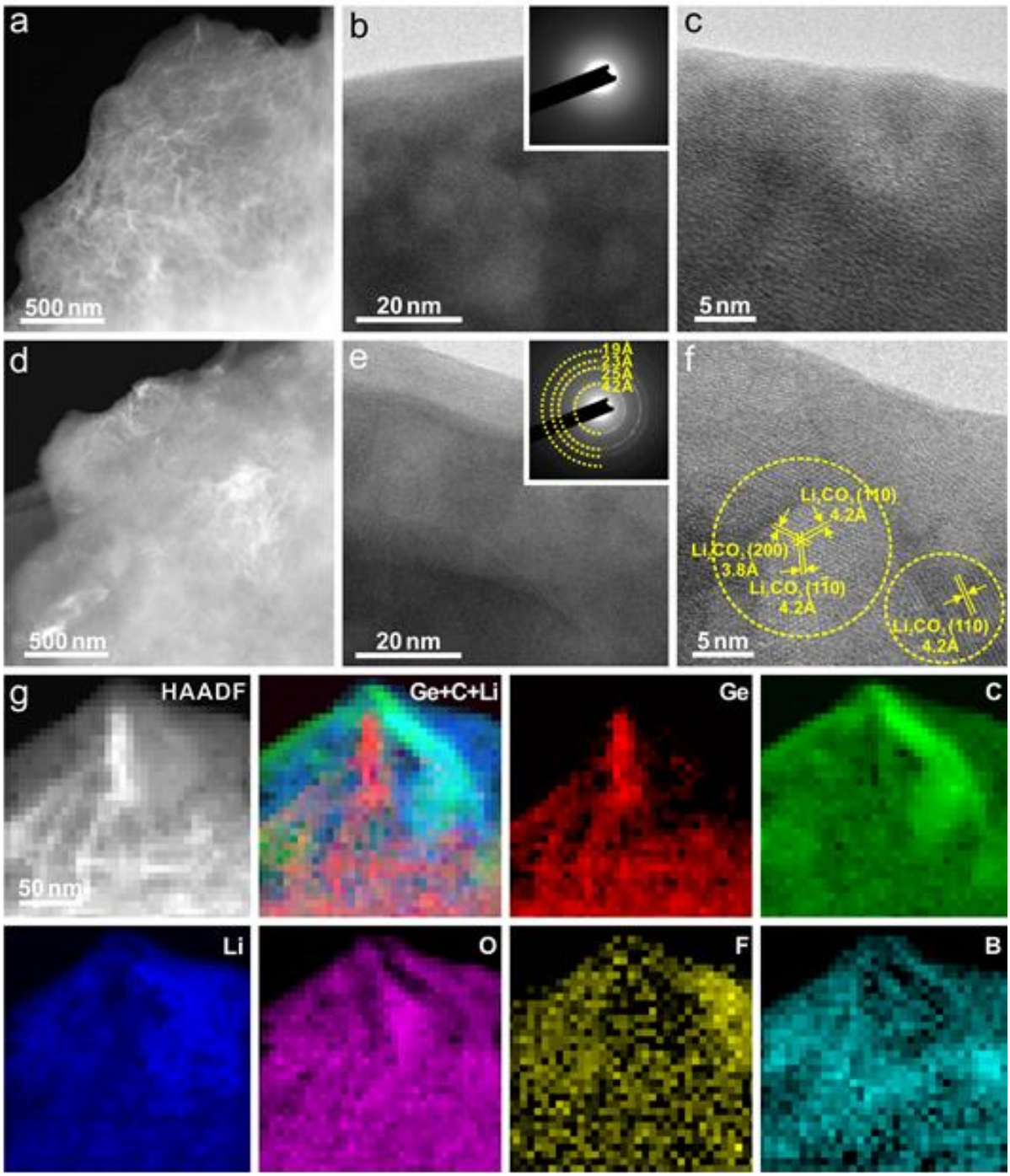

Fig. 5. Composition/nanostructure of SEIs after 50 cycles probed by cryo-TEM. (a-f) High-angle annular dark-field (HAADF) STEM and TEM images of SEIs in (a-c) LiDFOB and (d-

f) $LiPF_6$ electrolytes with SAED as insets in (b, e). Note that (c) and (f) are the enlarged HRTEM images for the SEI layer region. (g) HAADF-STEM image, EELS mapping with the averaged composition SEIs in LiDFOB electrolyte.

3.4. Full cell evaluation

A Li-ion full cell is constructed to demonstrate the feasibility of the practical application of a Ge anode and the compatibility of LiDFOB electrolyte with a cathode. A commercially available $LiCoO_2$ is adopted as the cathode. It shows a stable capacity of 135 mAh g^{-1} with an average discharge voltage of 3.89 V (**Fig. S13**). Coupling with a Ge anode, a 3.34 V class LIB would be obtained (**Fig. 6a**). **Fig. 6b** presents the charge and discharge curves at the first three cycles of the $LiCoO_2$-Ge full cell in LiDFOB electrolyte. The cell has an initial charge capacity of 161 mAh g^{-1}, but only 126 mAh g^{-1} is recovered in the discharge owing to the consumption of Li ions during SEI formation on the Ge anode surface. The discharge profiles resemble those of the initial one in the subsequent cycles, indicative of the reversible insertion/extraction process. Under the traditional $LiPF_6$ electrolyte, the full cell has analogous voltage profiles, suggesting variation of salt does not change the electrochemical reactions (**Fig. S14**). Nevertheless, the full cell using LiDFOB delivers much better cyclic stability. A high residual capacity of 106 mAh g^{-1} after 100 cycles is obtained based on $LiCoO_2$ with the areal loading of ~5.9 mg cm^{-2}, corresponding to a capacity retention of 84%, as shown in **Fig. 6c**. The results verify that LiDFOB electrolyte is fully compatible with a commercial cathode, while possessing significant advantages in stabilizing the anodes.

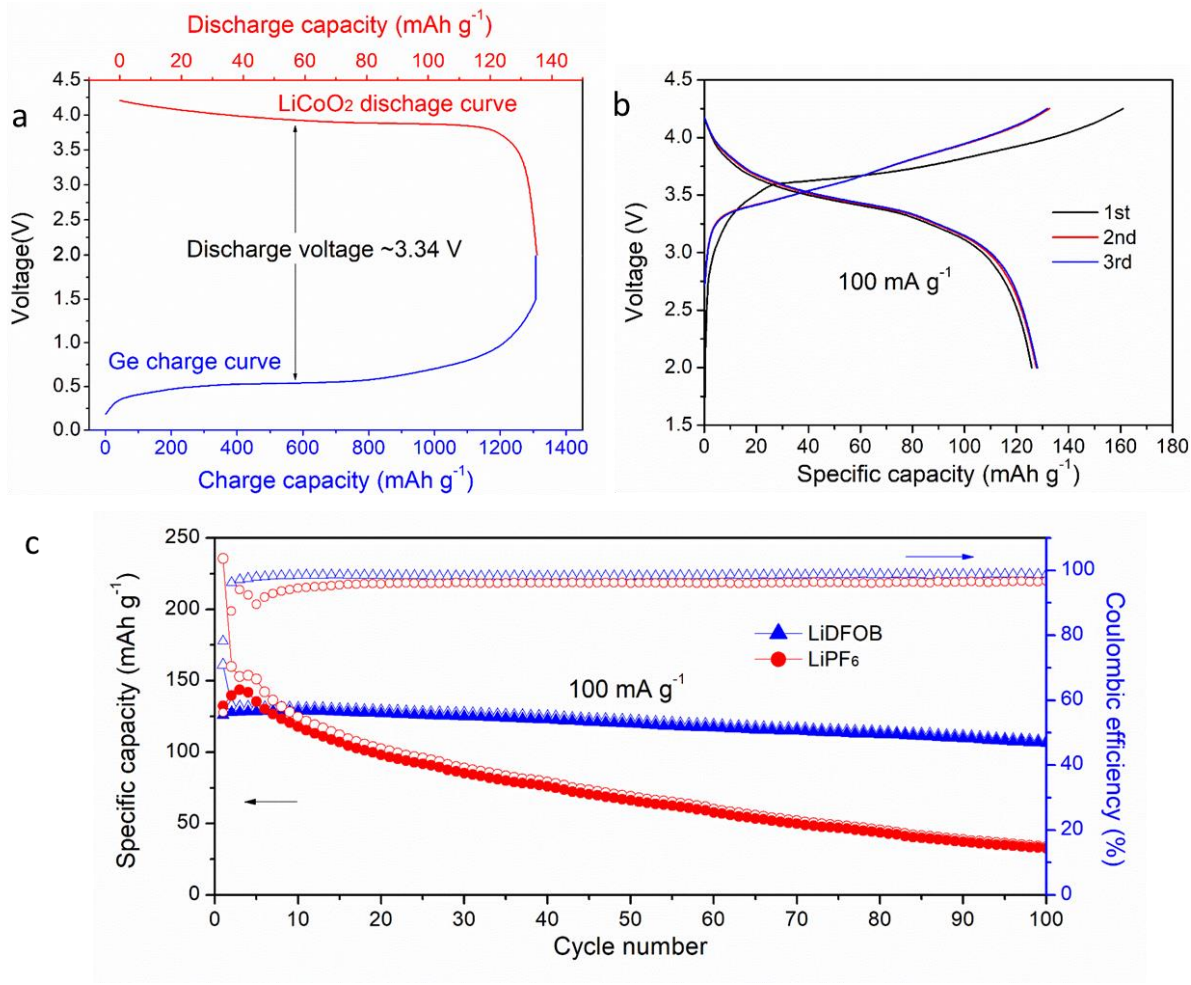

Fig. 6. Full cell examination. (a) Illustration of the full cell operation by adopting the charge and discharge curves of half Ge and $LiCoO_2$ cells, respectively; (b) charge and discharge curves of a full Ge-$LiCoO_2$ battery in LiDFOB electrolyte; (c) cyclic performance of full Ge-$LiCoO_2$ batteries in LiDFOB and $LiPF_6$ electrolytes.

4. Conclusions

Tuning the microstructure of alloy anodes is essential for providing sufficient free space to accommodate the volume expansion. Rather than design a porous electrode, we utilize the pores generated during the de-lithiation process to stabilize the Ge anode. It reveals the microstructure evolution is closely related to the SEI. The replacement of classic $LiPF_6$ salt by LiDFOB leads to the formation of unique SEI, consisting of amorphous inorganic particles

embedded in the organic matrix. Such a structure significantly improves the ionic conductivity at the interphase, assisting the development of abundant nanopores as demonstrated by the STEM. As a consequence, the Ge anode sustains a capacity of 1211 mAh g^{-1} after 200 cycles, even with a microsized particle of 1.4 μm on average. Application-wise, the strategy adopted here is fully compatible with a full cell, thus promoting the application of microsized Ge anodes.

Acknowledgments

This work was financially supported by the Key Project for Basic Research of Shenzhen (No. JCYJ20170818104125570), the Research Grant Council of Hong Kong (GRF project: 15305219), and the Hong Kong Polytechnic University (Area of Excellence Project 1-ZE30).

References

[1] W. J. Zhang, A review of the electrochemical performance of alloy anodes for lithium-ion batteries. J. Power Sources. 196 (2011) 13–24.

[2] H. Kim, Y. Son, C. Park, J. Cho, H. C. Choi, Catalyst-free direct growth of a single to a few layers of graphene on a germanium nanowire for the anode material of a lithium battery. Angew. Chem. Int. Ed. 52 (2013) 5997–6001.

[3] X. Li, Z. Yang, Y. Fu, L. Qiao, D. Li, H. Yue, D. He, Germanium anode with excellent lithium storage performance in a germanium/lithium–cobalt oxide lithium-ion battery. ACS Nano 9(2) (2015) 1858–1867.

[4] S. Zhang, Y. Zheng, X. Huang, J. Hong, B. Cao, J. Hao, Q. Fan, T. Zhou, Z. Guo, Structural engineering of hierarchical micro- nanostructured Ge-C framework by controlling the nucleation for ultralong- life Li storage. Adv. Energy Mater. (2019) 1900081.

[5] W. Hong, A. Wang, L. Li, T. Qiu, J. Li, Y. Jiang, G. Zou, H. Peng, H. Hou, X. Ji, Bi dots confined by functional carbon as high- performance anode for lithium ion batteries. Adv. Funct.

Mater. (2020) 2000756.

[6] W. Ai, Z. Huang, L. Wu, Z. Du, C, Zou, Z. He, R. Shahbazian-Yassar, W, Huang, T. Yu, High-rate, long cycle-life Li-ion battery anodes enabled by ultrasmall tin-based nanoparticles encapsulation. Energy Stor. Mater. 14 (2018) 169-178.

[7] B. Zhang, J. Huang, J. K. Kim, Ultrafine amorphous SnO_x embedded in carbon nanofiber/carbon nanotube composites for Li-ion and Na-ion batteries. Adv. Funct. Mater. 25 (2015) 5222-5228.

[8] B. Zhang, Y. Yu, Z. Huang, Y. He, D. Jang, W. Yoon, Y. Mai, F. Kang, J. K. Kim, Exceptional electrochemical performance of freestanding electrospun carbon nanofiber anodes containing ultrafine SnO_x particles. Energy Environ. Sci. 5 (2012) 9895–9902.

[9] Y. Li, K. Yan, H. Lee, Z. Lu, N. Liu, Y. Cui, Growth of conformal graphene cages on micrometre-sized silicon particles as stable battery anodes. Nat. Energy 1 (2016) 15029.

[10] S. Choi, T. Kwon, A. Coskun, J. W. Choi, Highly elastic binders integrating polyrotaxanes for silicon microparticle anodes in lithium ion batteries. Science 283 (2017) 279–283.

[11] R. Zhang, J. Bao, Y. Wang, S. C. Sun, Concentrated electrolytes stabilize bismuth–potassium batteries. Chem. Sci. 9 (2018) 6193–6198.

[12] B. Zhang, G. Rousse, D. Foix, R. Dugas, D. Alves, D. Corte, J. M. Tarascon, Microsized Sn as advanced anodes in glyme-based electrolyte for Na-ion batteries. Adv. Mater. 28 (2016) 9824–9830.

[13] J. Huang, X. Guo, X. Du, X. Lin, J. Huang, H. Tan, Y. Zhu, B. Zhang, Nanostructures of solid electrolyte interphases and their consequences for microsized Sn anodes in sodium ion batteries. Energy Environ. Sci.12 (2019) 1550–1557.

[14] J. Huang, X. Lin, H. Tan, B. Zhang, Bismuth microparticles as advanced anodes for potassium-ion battery. Adv. Energy Mater. (2018) 1703496.

[15] K. Lei, C. Wang, L. Liu, Y. Luo, C. Mu, F. Li, J. Chen, A porous network of bismuth used

as the anode material for high- energy- density potassium- ion batteries. Angew. Chem. Int. Ed. 57 (2018) 4687–4691.

[16] J. Chen, X. Fan, Q. Li, H. Yang, M. R. Khoshi, Y. Xu, S. Hwang, L. Chen, X. Ji, C. Yang, H. He, C. Wang, E. Garfunkel, D. Su, O. Borodin, C. Wang, Electrolyte design for LiF-rich solid–electrolyte interfaces to enable high-performance microsized alloy anodes for batteries. Nat. Energy (2020) 1–12.

[17] X. H. Liu, S. Huang, S. T. Picraux, J. Li, T. Zhu, J. Y. Huang, Reversible nanopore formation in Ge nanowires during lithiation–delithiation cycling: an in situ transmission electron microscopy study. Nano Lett. 11 (2011) 3991–3997.

[18] X. Zhou, T. Li, Y. Cui, M. L. Meyerson, C. B. Mullins, Y. Liu, L. Zhu, In situ focused ion beam-scanning electron microscope study of crack and nanopore formation in germanium particle during (de)lithiation. ACS Appl. Energy Mater. 2 (2019) 2441−2446.

[19] B. Zhang, G. Rousse, D. Foix, R. Dugas, D. A. D. Corte, J. M.Tarascon, Microsized Sn as advanced anodes in glyme-based electrolyte for Na-ion batteries. Adv. Mater. 28 (2016) 9824–9830.

[20] X. Du, J. Huang, X. Guo, X. Lin, J. Q. Huang, H. Tan, Y. Zhu, B. Zhang, Preserved layered structure enables stable cyclic performance of MoS_2 upon potassium insertion. Chem. Mater. 31 (2019) 8801−8809.

[21] B. Zhang, Y. Liu, Z.D. Huang, S.W. Oh, Y. Yu, Y.W. Mai, J. K. Kim, Urchin-like $Li_4Ti_5O_{12}$–carbon nanofiber composites for high rate performance anodes in Li-ion batteries. J. Mater Chem. 22 (2012) 12133−12140.

[22] B. Zhang, F. Kang, J. M. Tarascon, J. K. Kim, Recent advances in electrospun carbon nanofibers and their application in electrochemical energy storage. Progress Mater. Sci. 76 (2016) 319-380.

[23] L. Chen, X. Fan, E. Hu, X. Ji, J. Chen, S. Hou, T. Deng, J. Li, D. Su, X. Yang, C. Wang,

Achieving high energy density through increasing the output voltage: a highly reversible 5.3 V battery. Chem 5 (2019) 896–912.

[24] H. Gao, F. Maglia, P. Lamp, K. Amine, Z. Chen, Mechanistic study of electrolyte additives to stabilize high-voltage cathode–electrolyte interface in lithium-ion batteries. ACS Appl. Energy Mater. 9 (2017) 44542−44549.

[25] S. Jurng, Z. L. Brown, J. Kim, B. L. Lucht, Effect of electrolyte on the nanostructure of the solid electrolyte interphase (SEI) and performance of lithium metal anodes. Energy Environ. Sci. 11 (2018) 2600−2608.

[26] Z. Chang, X. Li, F. Yun, Z. Shao, Z. Wu, J. Wang, S. Lu. The effect of dual-salt concentrated electrolytes on the electrochemical performance of silicon nanoparticles. ChemElectroChem. 7 (2020) 1135-1141.

[27] F. An, H. Zhao, W. Zhou, Y. Ma, P. Li. S-containing and Si-containing compounds as highly effective electrolyte additives for SiO_x -based anodes/NCM 811 cathodes in lithium ion cells. Sci. Rep. 9 (2019) 14108.

[28] X. Ou, G. Zhang, S. Zhang, X. Tong, Y. Tang. Simultaneously pre-alloying and artificial solid electrolyte interface towards highly stable aluminum anode for high-performance Li hybrid capacitor. Energy Storage Mater. 28 (2020) 357-363.

[29] A. L. Michan, M. Leskes, C. P. Grey, Voltage dependent solid electrolyte interphase formation in silicon electrodes: monitoring the formation of organic decomposition products. Chem. Mater. 28 (1) (2016) 385-398.

[30] L. C. Loaiza, N. Louvain, B. Fraisse, A. Boulaoued, A. Iadecola, P. Johansson, L. Stievano, V. Seznec, L. Monconduit, Electrochemical lithiation of Ge: new insights by operando spectroscopy and diffraction. J. Phys. Chem. C 122 (2018) 3709−3718.

[31] M. D. Levi, D. Aurbach, Simultaneous measurements and modeling of the electrochemical impedance and the cyclic voltammetric characteristics of graphite electrodes doped with

lithium. J. Phys. Chem. B 5647 (1997) 4630–4640.

[32] G. Assat, C. Delacourt, D. Alves, D. Corte, J. M. Tarascon, Editors' choice—practical assessment of anionic redox in Li-rich layered oxide cathodes: a mixed blessing for high energy Li-ion batteries. J. Electrochem. Soc. 163 (2016) A2965-A2976.

[33] R. Dedryvere, L. Gireaud, S. Grugeon, S. Laruelle, J. M. Tarascon, D. Gonbeau, Characterization of lithium alkyl carbonates by X-ray photoelectron spectroscopy: experimental and theoretical study. J. Phys. Chem. B 109 (2005) 15868-15875.

[34] Y. Li, Y. Li, A. Pei, K. Yan, Y. Sun, C. Wu, L. M. Joubert, R. Chin, A. L. Koh, J. Perrino, B. Butz, S. Chu, Y. Cui, Atomic structure of sensitive battery materials and interfaces revealed by cryo–electron microscopy. Science 510 (2017) 506–510.

[35] F. Tian, M. D. Radin, D. J. Siegel, Enhanced charge transport in amorphous Li_2O_2. Chem. Mater. 26 (2014) 2952–2959.